

Tunable magnon-magnon coupling in synthetic antiferromagnets

A. Sud,^{1,*} C. W. Zollitsch,¹ A. Kamimaki,^{2,3} T. Dion,¹ S. Khan,¹ S. Iihama,^{4,5} S. Mizukami,^{3,5,6} and H. Kurebayashi^{1,†}

¹London Centre for Nanotechnology, University College London, London WC1H 0AH, United Kingdom

²Department of Applied Physics, Tohoku University, Aoba 6-6-05, Sendai, 980-8579, Japan

³WPI Advanced Institute for Materials Research,

Tohoku University, 2-1-1, Katahira, Sendai 980-8577, Japan

⁴Frontier Research Institute for Interdisciplinary Sciences, Tohoku University, Sendai 980-8578, Japan

⁵Center for Spintronics Research Network, Tohoku University, Sendai, 980-8577, Japan

⁶Center for Science and Innovation in Spintronics, Tohoku University, Sendai, 980-8577, Japan

In this work, we study magnon-magnon coupling in synthetic antiferromagnets (SyAFs) using microwave spectroscopy at room temperature. Two distinct spin-wave modes are clearly observed and are hybridised at degeneracy points. We provide a phenomenological model that captures the coupling phenomena and experimentally demonstrate that the coupling strength is controlled by the out-of-plane tilt angle as well as the interlayer exchange field. We numerically show that a spin-current mediated damping in SyAFs plays a role in influencing the coupling strength.

Generating new spin-wave states can be an enabling role for developing future spintronic/magnonic devices¹. While individual spin-wave modes can be tailored by changing material parameters of host magnets, a novel approach of creating new spin-wave states is to couple two modes coherently by tuning them into resonance, where physical parameters of the coupled modes can also be modified. Although the coupling phenomena could be phenomenologically explained by a classical coupled-oscillator picture in general, microscopic descriptions of this type of hybridisation are rich, offering novel functionalities of state control and energy/information transfer. For example, strong coupling of light-matter interaction is envisaged to offer fast and protected quantum information processing²⁻⁴. Within this expanding research domain, strong coupling between microwave photons and collective spins in magnetically-ordered systems has been extensively studied in recent years⁵⁻⁸.

Magnon-magnon coupling has an advantage over the light-matter interaction, in terms of coupling strength. The coupling strength of light-matter interactions is sometimes significantly reduced by a lack of spatial mode overlapping of the two, and so scientists have made considerable efforts to achieve large coupling strength by designing optimum geometries for efficient mode-volume overlapping^{9,10}. On the other hand, magnon-magnon interaction does not suffer from this since two modes normally reside within the same host media, providing mode overlapping of 100% or close to. While magnon-magnon coupling has been studied in single magnets^{5,11} and magnetic bi-layers^{13,14}, magnon-magnon interaction in highly tunable material systems could offer unexplored parameter spaces on which to tailor the coupling phenomena. Here, we focus on synthetic antiferromagnets (SyAFs) as a host of magnon-magnon coupling and report clear hybridisation of two distinct SyAF modes arising from interlayer exchange coupling between two magnetic layers. We provide a full phenomenological model for the mode coupling, magnetic relaxation and coupling strength as a function of different material parameters for

SyAF modes. Aided by these derived relationships, we demonstrate that the interlayer exchange field strength, which can be controlled by sample growth, allows the engineering of the coupling strength. We further numerically show that the spin-current mediated damping plays a role in influencing the coupling strength. Our demonstration and full details of the magnon-magnon coupling phenomena in SyAFs will act as a springboard for further research along this avenue¹⁵.

Low-energy spin-wave modes in synthetic antiferromagnets in their canted regime are acoustic and optical modes^{16,17} where two coupled moments precess in-phase (acoustic) and out-of-phase (optical) as shown in Fig. 1(a). The acoustic (optical) mode is excited by perpendicular (parallel) configuration between microwave and applied magnetic fields. There are a number of reports in which these two modes in different SyAFs have been studied in great detail^{7,17-19,21,22}. For example, mutual spin pumping within the coupled moments has been proposed^{6,23,24} and experimentally demonstrated²⁶⁻²⁹. Since the resonant frequency of two modes shows different magnetic field dependence (as discussed more later), we can find the degeneracy point of the two modes by tuning experimental conditions. When the two moments are canted within the plane, the motion of the optical and acoustic modes can be decoupled⁵, meaning that the two modes are not allowed to hybridise. This restriction can be lifted when we tilt the moments towards the out-of-plane direction and we will be able to hybridise them (see Fig.1(b) for schematic understanding). The strength of hybridisation is defined by g which represents a rate of energy transfer between the two modes. When this rate is fast, compared to mode dissipation rates of individual modes, we expect well-defined coupled modes before the excited states are relaxed. Control of the coupling strength *in-situ* and *ex-situ* will be potentially useful to a scheme of reconfigurable energy and information transfer using coherent coupling.

The SyAF stacked films used in this study were prepared by magnetron co-sputtering at a base pressure of

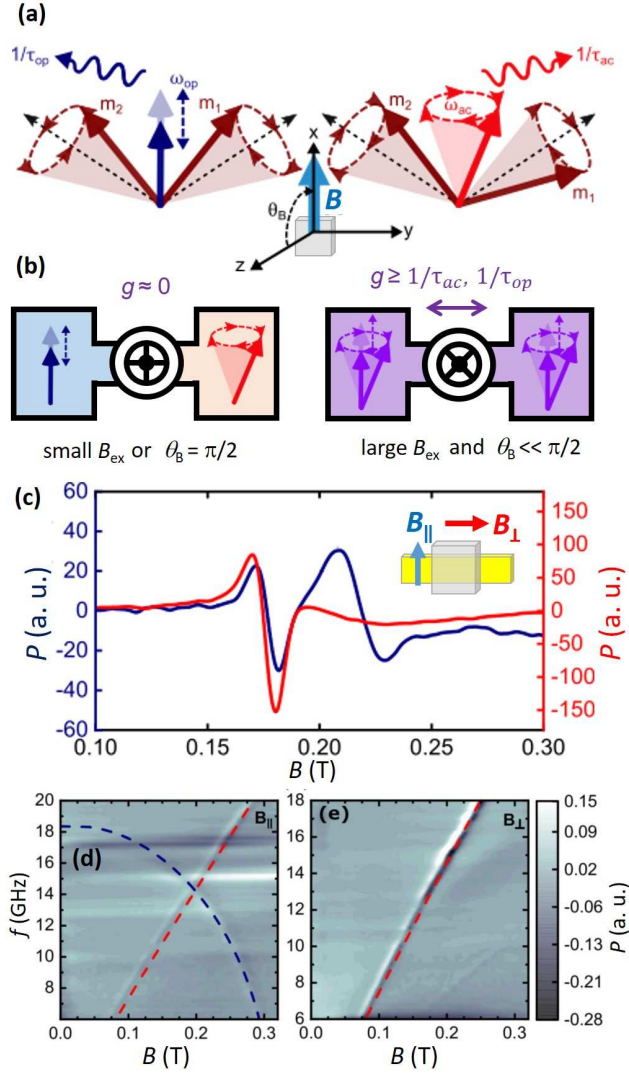


FIG. 1. (a) Schematic of acoustic and optical modes in SyAFs. Two moments (m_1 and m_2) are coupled antiferromagnetically and canted at equilibrium. Under microwave irradiation, they precess in-phase (acoustic mode) and out-of-phase (optical mode) at different angular frequencies ω_{ac} and ω_{op} , respectively. We define θ_B as in the figure, where the z axis is the film growth direction. (b) Schematics of the magnon-magnon coupling phenomena with the optical and acoustic modes. When the exchange field (B_{ex}) is small or two moments are within the film plane, the coupling strength (g) is zero, so the two modes do not couple. We can tune the coupling strength by tuning B_{ex} and θ_B and achieve strong magnon-magnon hybridisation, as shown on the right panel. (c) Microwave absorption spectrum for $\theta_B = 90^\circ$, measured at 13.4 GHz. Two magnetic field directions ($B_{||}$ and B_{\perp}) are defined as per the inset. Microwave transmission spectrum as a function of frequency and applied field for two configurations of applied magnetic fields (d) $B_{||}$ and (e) B_{\perp} for $\theta_B = 90^\circ$. Best fit curves using Eq. (1) and (2) represent as dashed curves in blue and in red, respectively.

1×10^{-7} Pa. The films were grown on a Si oxide substrate with the stacking pattern of Ta(3 nm)/CoFeB(3 nm)/Ru(t nm)/CoFeB(3 nm)/Ta(3 nm) where Ru thickness was varied to tune the interlayer exchange coupling⁷. Vibrating sample magnetometer (VSM) was used to characterise the static magnetic properties (see Supplemental Material). These sample chips were placed on a coplanar waveguide board to perform broadband spin dynamics characterisation. For each measurement, we fixed the frequency and swept a dc external magnetic field with an ac modulation component at 12 Hz. Figure 1(c) shows typical measurement curves for two field directions ($B_{||}$ and B_{\perp}) defined by the figure inset. We carried out systematic experiments for a wide range of frequency (5-20 GHz) as well as field angle to study mode hybridisation and linewidth evolution of SyAFs. To extract the peak position and linewidth, we used derivative Lorentzian functions³⁰. Figures 1(d)-(e) show two-dimensional color plots of microwave absorption as a function of microwave frequency and magnetic field. We can clearly identify two modes in Fig. 1(d) for the $B_{||}$ condition whereas only one in Fig. 1(e) for B_{\perp} . This is because for $B_{||}$, both modes can be excited since microwave rf fields have components of both parallel and perpendicular to $B_{||}$ due to their spatial distribution above the waveguide. For B_{\perp} measurements, the microwave magnetic field only possesses components perpendicular to B_{\perp} , hence only exciting the acoustic mode. In order to analyse these results quantitatively, we solve a coupled Landau-Lifshitz-Gilbert (LLG) equation with small angle approximation^{5,31-33} (see Supplemental Material for more details) and find the resonance condition of the two modes as:

$$\omega_{ac} = \gamma B_0 \sqrt{\left(1 + \frac{B_s}{2B_{ex}}\right)}, \quad (1)$$

$$\omega_{op} = \gamma \sqrt{2B_{ex}B_s \left(1 - \left(\frac{B_0}{2B_{ex}}\right)^2\right)}, \quad (2)$$

Here, B_{ex} , B_s , B_0 and γ are the exchange field, the demagnetisation magnetization, the resonance field and the gyromagnetic ratio, respectively. We found that our best fits produce B_{ex} , B_s and $\gamma/2\pi$ to be 0.14 T, 1.5 T and 29 GHz/T respectively. Fits using Eqs. 1 and 2 can reproduce our experimental results very well, strongly supporting that we can experimentally observe and study the coupled SyAF modes. Since the frequency of the two modes show different magnetic field dependences, it is possible to study mode coupling of the two by tuning the mode frequencies. In Fig. 1(d), we observe a clear crossing of the two modes at $B_0 \approx 0.2$ T. This "crossing" means that the two modes are not able to hybridise due to mode symmetry⁵. We can break this symmetry by tilting the moment towards the out-of-plane direction. We therefore repeated similar experiments for $\theta_B \neq 90^\circ$ as shown in Fig. 2(a-c). The two modes start to show an avoided crossing as θ_B is decreased, indicating mode

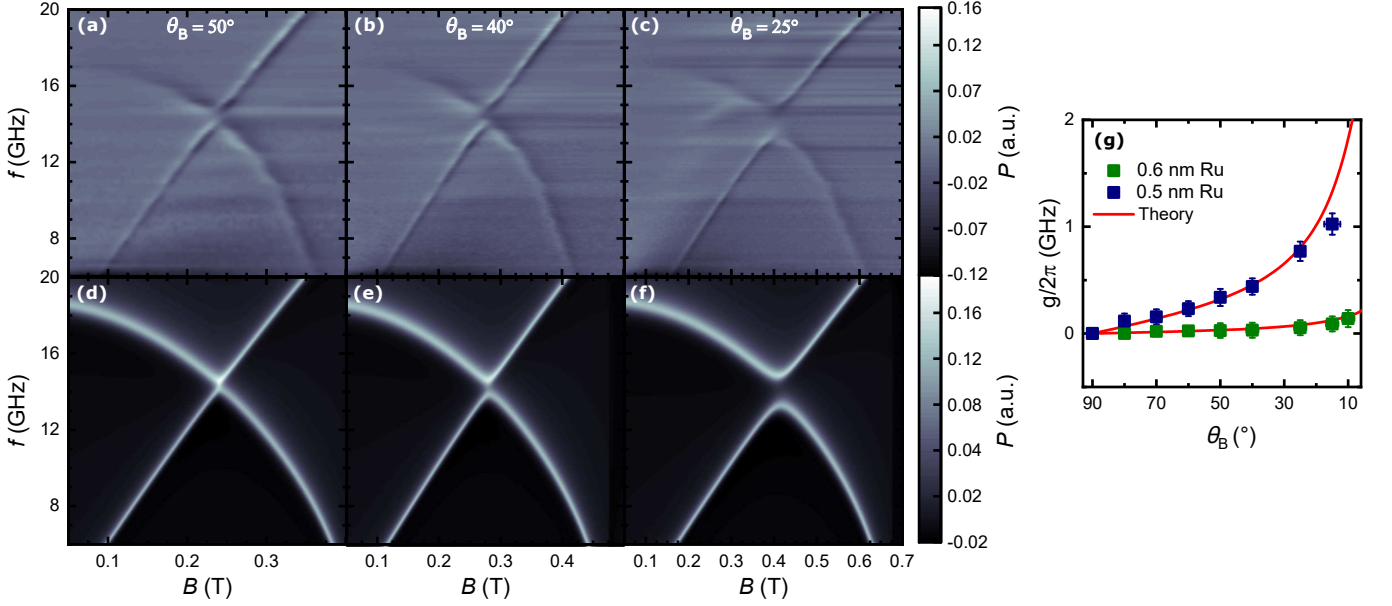


FIG. 2. (a-c) Microwave transmission as a function of frequency and applied field for different θ_B . The avoided crossing starts to appear and the frequency gap increases as θ_B is decreased. (d)-(f) Simulation results for the same experimental condition as (a)-(c), respectively. (g) The coupling strength $g/2\pi$ as a function of θ_B . We plot results from two samples with the Ru thickness of 0.5 nm and 0.6 nm. The 0.5 nm sample shows sizable $g/2\pi$, compared to much smaller $g/2\pi$ for 0.6 nm. The red curves are produced by Eq. (3) in the main text.

hybridisation which can be quantitatively discussed by using the coupling strength $g/2\pi$, the half of the minimum frequency gap. We plot the θ_B dependence of $g/2\pi$ in Fig. 2(g) where $g/2\pi$ grows with the out-of-plane component, with the highest value exceeding 1 GHz.

We describe the magnon-magnon coupling phenomena in SyAFs by a 2×2 matrix eigenvalue problem derived from the coupled LLG equations with mutual spin pumping terms⁶ (see Supplemental Material for detailed derivation):

$$\begin{bmatrix} \omega^2 - \omega_{\text{op}}^2 + i(\nu_{\text{o1}} + \nu_{\text{o2}})\omega & (i\omega - \nu_{\text{o1}}\gamma B_s)\eta m_{z0} \\ (-i\omega + \nu_{\text{a2}}\gamma B_s)\eta m_{z0} & \omega^2 - \omega_{\text{ac}}^2 + i(\nu_{\text{a1}} + \nu_{\text{a2}})\omega \end{bmatrix}$$

Here, $\eta = 2B_{\text{ex}}/B_s$, $m_{z0} = B_0 \cos\theta_B / (B_s + 2B_{\text{ex}})$, $\nu_{\text{o1}} = (\alpha_0 + \alpha_{\text{sp}})(1 - m_{z0}^2) - \alpha_{\text{sp}}\{1 - m_{z0}^2 - (B_0^2 \sin^2\theta_B / 4B_{\text{ex}}^2)\}(m_{z0}^2/m^2)$, $\nu_{\text{o2}} = \alpha_0\eta(1 - B_0^2 \sin^2\theta_B / 4B_{\text{ex}}^2)$, $\nu_{\text{a1}} = \alpha_0\eta(m_{z0}^2 + B_0^2 \sin^2\theta_B / 4B_{\text{ex}}^2)$ and $\nu_{\text{a2}} = \alpha_0(\eta + 1)(1 - m_{z0}^2)$, respectively, with α_0 and α_{sp} being the standard Gilbert damping constant and one arising from mutual spin pumping between the two magnetic layers. The real part of the eigenvalues gives the resonance frequencies and the imaginary part represents the loss rates of the two modes. We numerically solved the eigenvalue problem with parameters described above and found that the coupled equations can model our experimental observation well for each experimental set, such as Figs. 2 (d)-(f) reproducing corresponding experimental results. We simplified the 2×2 matrix by neglecting the damping terms to calculate the eigenvalues and found an analytical expression for the coupling strength as (see derivation in Supplemental Material):

$$g = \frac{\gamma B_{\text{ex}} B_0}{2B_s + 4B_{\text{ex}}} \cos\theta_B. \quad (3)$$

This correctly captures our experimental observation as $g/2\pi$ grows with decreasing θ_B . The red curve in Fig. 2(g) is calculated by this equation and there is quantitative agreement between experiments and theory, despite marginal deviation at small θ_B . To further attest the validity of this equation for our experiments, we performed similar measurements on a SyAF sample having the Ru thickness of 0.6 nm since Eq. 3 suggests that the coupling strength can be tuned by B_{ex} . For this sample, we found that B_{ex} is decreased to 30 mT due to a weaker inter-layer coupling and accordingly, as expected, we observed a significant decrease of $g/2\pi$ as summarised in Fig. 2(g). These results show the tunability of the mode coupling strength in SyAFs by both thin-film growth engineering (*ex-situ*) as well as out-of-plane tilt angle (*in-situ*).

Next we focus on the relaxation of the SyAF modes. Figure 3(a-b) represent plots of the half width at half maximum (HWHM) linewidth (ΔB) extracted for individual sweeps for both modes. ΔB of the acoustic mode increases with increasing magnetic field, with a characteristic anomaly around the field where the two modes hybridise. ΔB of the optical mode however shows a different magnetic field dependence as it decreases with increasing magnetic field. This is primarily due to the relationship of the magnetic-field-domain linewidth and

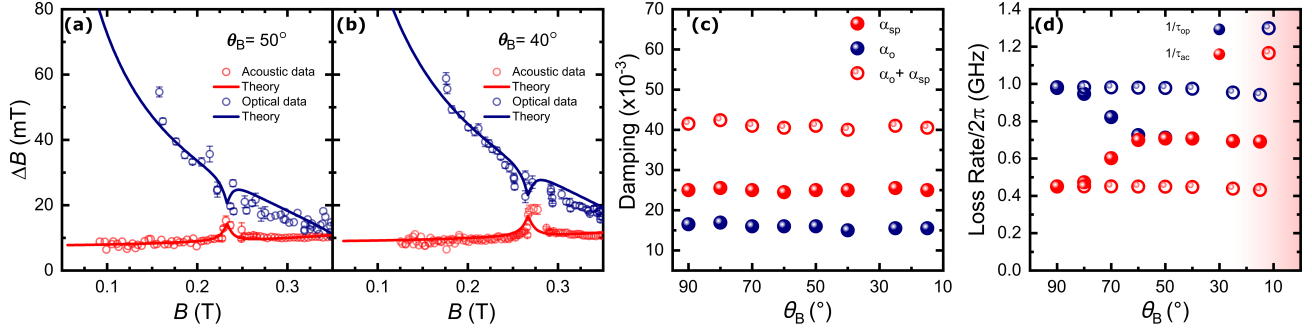


FIG. 3. (a-c) HWHM linewidth as a function of magnetic field for θ_B of (a) 50° and (b) 40° . solid lines represent results from the theoretical model discussed in the main text. (c) Extracted values of damping parameters. (d) Calculated loss rates of each mode at the crossing point as well as those of the hybridised modes.

frequency-domain linewidth as given by:

$$\Delta B_{\text{Op(ac)}} = \left| \frac{d\omega_{\text{op(ac)}}}{dB} \right|^{-1} \frac{1}{\tau_{\text{op(ac)}}}. \quad (4)$$

When the resonance field is low, $|d\omega_{\text{op}}/dB|$ becomes small, which can extrinsically enhance the observed ΔB in our experiments. In order to extract material-specific parameters such as α_0 from our data, we solved the eigenvalue problem and compared the imaginary part with experimental results. We found that the linewidth calculated from the imaginary part models excellently for our experiments as shown in Fig. 3(a)-(b). Extracted α_0 and α_{sp} for different θ_B are plotted in Fig. 3 (c). We can confirm that there is a sizable spin pumping component for every angle we measured, in consistent with previous reports^{6,7,28,34}. The Ru thickness is much shorter than its spin diffusion length of 14 nm³⁵. As a result, when two ferromagnets are precessing in-phase, according to spin pumping theory³⁶, spin currents flowing out of the two are cancelled out hence developing zero time-dependent spin accumulation in the Ru layer. However, when two moments precess out of phase, the emitted spin currents no longer cancel out, leading to the spin-accumulation which induces an additional damping mechanism for the optical mode. In our experiments, we observe that both α_0 and α_{sp} are independent of θ_B , which can be understood that the Gilbert damping components are a material parameter, independent of experimental conditions - note here that the canted angle has been already taken into account in the expressions.

An interesting observation is that the experimentally deduced ΔB for both modes also show "attraction" around the avoided crossing points. This demonstrates that magnetic relaxation can be modified by mode coupling phenomena. In the crossing regime, two modes are no longer pure acoustic or optical and therefore it is not possible to use the ac spin pumping picture associated with the phase difference between two moments. Rather, a simple phenomenological picture of hybridised energy losses would be a better one. When two modes with

different loss rates start to couple coherently, their loss rates also start to merge together³⁷. This is because the energy transfer mixes the two loss rates since the high (low)-loss mode becomes the low(high)-loss mode as a function of time. We are able to observe this feature in our experiments. This loss rate hybridisation is reproduced by our numerical simulations from the eigenvalue problem as shown in Figs. 3(a-b). This linewidth averaging is similar to ones discussed in spin-photon coupling systems^{38,39}. We went on to quantify the loss rates for both modes by using Eq. 4. First of all, we estimated the loss rate of individual modes at the avoided crossing point (open circles in Fig. 3 (d)), by extrapolating from the values outside the coupling regime. Both show a very weak angular dependence, which can be understood that the damping (Fig.3 (c)) has no angular dependence with a subtle change of the mode-crossing frequency when θ_B is decreased. By contrast, loss rates for the hybridised modes (solid circles in Fig. 3 (d)), estimated by our eigenvalue problem, exhibit clear attraction as the coupling strength is increased by changing θ_B . After $\theta_B = 60^\circ$, the loss rates of the two modes coalesce into a single number which is exactly the average of the two rates $1/\tau_{\text{mix}} = (1/2)(1/\tau_{\text{ac}} + 1/\tau_{\text{op}})$ where $1/\tau_{\text{mix}}$ is the loss rate of the hybridised states. Furthermore, through the course of our simulation study, we found that α_{sp} can have an effect on g , suggesting that the magnon-magnon coupling is partially mediated by spin currents. We observe that for large α_{sp} the coupling between the two modes can be completely suppressed (see Supplemental Material). We highlight that this damping-mediated coupling control cannot be achieved by simply changing α_0 in our system, something specific for the magnetic relaxation via spin pumping to the coupling and the energy exchange. Although it is not possible to control α_{sp} in our experiments, it could act as an extra parameter to define the magnon-magnon coupling strength in SyAFs. Finally, we highlight that the highest $g/2\pi$ achieved (1.0 GHz) outnumbers the loss rates of the individual modes, indicating that this magnon-magnon coupling starts to

enter the strong coupling regime in our experiments. Although our experiments are just at the onset of the strong coupling regime, here we briefly discuss potential improvements and control of the coupling strength against the individual loss rates. Equation (3) can be simplified as $g/2\pi \propto B_{\text{ex}}/B_s$, suggesting that a sample with a higher B_{ex} as well as a smaller B_s shows a large coupling strength. Achieving similar coupling with low-damping materials could be another plausible path.

In summary, we experimentally show the magnon-magnon coupling in SyAF CoFeB/Ru/CoFeB multilayers. Clear magnon-magnon hybridisation has been observed when the optical and acoustic modes are tuned into resonance. The magnon-magnon coupling strength has been controlled by bringing the moments into the

out-of-plane direction, which breaks the orthogonality of the two modes. In addition, the interlayer exchange coupling is found to tune the coupling strength. The loss rate of two modes exhibits an averaging effect upon hybridisation. Our eigenvalue problem approach serves to provide the analytical expression of the coupling strength as well as numerical explanations/predictions of the experimental data. We envisage that results in the present study will be transferable to other weakly-coupled antiferromagnetic systems since the phenomenological descriptions of their spin-wave modes should be identical to our model developed.

A.K. acknowledges the Graduate Program in Spintronics (GP-Spin) at Tohoku University. This work was supported in part by CSRN, CSIS and UCL-Tohoku Strategic Partner Funds.

* aakanksha.sud.17@ucl.ac.uk

† h.kurebayashi@ucl.ac.uk

- ¹ A. V. Chumak, V. I. Vasyuchka, A. A. Serga, and B. Hillebrands, *Nature Physics* **11**, 453461 (2015).
- ² A. F. Kockum, A. Miranowicz, S. D. Liberato, S. Savasta, and F. Nori, *Nat. Rev.Phys.* **1**, 19 (2019).
- ³ Z.-L. Xiang, S. Ashhab, J. Q. You, and F. Nori, *Rev. Mod. Phys.* **85**, 623 (2013).
- ⁴ A. A. Clerk, K. W. Lehnert, P. Bertet, J. R. Petta, and Y. Nakamura, *Nat. Phys.* **16**, 257 (2020).
- ⁵ Lachance-Quirion, D. Tabuchi, A. Y., Gloppe, K. Usami, and Y. Nakamura, *Appl. Phys. Express* **12**, 070101 (2019).
- ⁶ M. Harder and C.-M. Hu, *Solid State Physics 69*, edited by R. E. Camley and R. L. Stamp (Academic Press, Cambridge, 2018) pp. 47–121.
- ⁷ H. Huebl, C. W. Zollitsch, J. Lotze, F. Hocke, M. Greifenstein, A. Marx, R. Gross, and S. T. B. Goennenwein, *Phys. Rev. Lett.* **111**, 127003 (2013).
- ⁸ X. Zhang, C. L. Zou, L. Jiang, and H. X. Tang, *Phys. Rev. Lett.* **113**, 156401 (2014).
- ⁹ C. Eichler, A. J. Sigillito, S. A. Lyon, and J. R. Petta, *Phys. Rev. Lett.* **118**, 037701 (2017).
- ¹⁰ G. Tosi, F. A. Mohiyaddin, H. Huebl, and A. Morello, *AIP Adv.* **4**, 087122 (2014).
- ¹¹ L. Liensberger, A. Kamra, H. Maier-Flaig, S. Geprags, A. Erb, S. T. Goennenwein, R. Gross, W. Belzig, H. Huebl, and M. Weiler, *Phys. Rev. Lett.* **123**, 117204 (2019).
- ⁵ D. MacNeill, J. T. Hou, D. R. Klein, P. Zhang, P. Jarillo-Herrero, and L. Liu, *Phys. Rev. Lett.* **123**, 047204 (2019).
- ¹³ J. Chen, C. Liu, T. Liu, Y. Xiao, K. Xia, G. E. Bauer, M. Wu, and H. Yu, *Phys. Rev. Lett.* **120**, 217202 (2018).
- ¹⁴ S. Klingler, V. Amin, S. Geprags, K. Ganzhorn, H. Maier-Flaig, M. Althammer, H. Huebl, R. Gross, R. D. McMichael, M. D. Stiles, S. T. B. Goennenwein, and M. Weiler, *Phys. Rev. Lett.* **120**, 127201 (2018).
- ¹⁵ R. A. Duine, K.-J. Lee, S. S. P. Parkin, and M. D. Stiles, *Nat. Phys.* **14**, 217 (2018).
- ¹⁶ F. Keffer and C. Kittel, *Physical Review* **85**, 329 (1952).
- ¹⁷ J. J. Krebs, P. Lubitz, A. Chaiken, and G. A. Prinz, *J. Appl. Phys.* **67**, 5920 (1990).
- ¹⁸ A. Konovalenko, E. Lindgren, S. S. Cherepov, V. Korenivski, and D. C. Worledge, *Phys. Rev. B* **80**, 144425

(2009).

- ¹⁹ T. Seki, H. Tomita, A. A. Tulapurkar, M. Shiraishi, T. Shinjo, and Y. Suzuk, *Appl. Phys. Lett.* **94**, 212505 (2009).
- ⁷ A. Kamimaki, S. Iihama, T. Taniguchi, and S. Mizukami, *Appl. Phys. Lett.* **115**, 132402 (2019).
- ²¹ W. Wang, P. Li, C. Cao, F. Liu, R. Tang, G. Chai, and C. Jiang, *Appl. Phys. Lett.* **113**, 042401 (2018).
- ²² M. Ishibashi, Y. Shiota, T. Li, S. Funada, T. Moriyama, and T. Ono, *Sci. Adv.* **6**, eaaz6931 (2020).
- ²³ T. Taniguchi and H. Imamura, *Phys. Rev. B* **76**, 092402 (2007).
- ²⁴ S. Takahashi, *Appl. Phys. Lett.* **104**, 052407 (2014).
- ⁶ T. Chiba, G. E. Bauer, and S. Takahashi, *Phys. Rev. B* **92**, 054407 (2015).
- ²⁶ A. A. Timopheev, Y. G. Pogorelov, S. Cardoso, P. P. Freitas, G. N. Kakazei, and N. A. Sobolev, *Phys. Rev. B* **89**, 144410 (2014).
- ²⁷ K. Tanaka, T. Moriyama, M. Nagata, T. Seki, K. Takanashi, S. Takahashi, and T. Ono, *Appl. Phys. Express* **7**, 063010 (2014).
- ²⁸ H. Yang, Y. Li, and W. E. Bailey, *Appl. Phys. Lett.* **108**, 242404 (2016).
- ²⁹ S. Sorokin, R. A. Gallardo, C. Fowley, K. Lenz, A. Titova, G. Y. P. Atcheson, G. Dennehy, K. Rode, J. Fassbender, J. Lindner, and A. M. Deac, *Phys. Rev. B* **101**, 144410 (2020).
- ³⁰ K. Rogdakis, A. Sud, M. Amado, C. M. Lee, L. McKenzie-Sell, K.-R. Jeon, M. Cubukcu, M. G. Blamire, J. W. A. Robinson, L. F. Cohen, and H. Kurebayashi, *Phys. Rev. Mater.* **3**, 014406 (2019).
- ³¹ P. Streit and G. E. Everett, *Phys. Rev. B* **21**, 169 (1980).
- ³² V. S. MANDEL, V. D. Voronkov, and D. E. Gromzin, *SOVIET PHYSICS JETP* **36**, 521 (1973).
- ³³ A. Kamimaki, S. Iihama, K. Z. Suzuki, N. Yoshinaga, and S. Mizukami, *Phys. Rev. Appl.* **13**, 044036 (2020).
- ³⁴ B. Heinrich, Y. Tserkovnyak, G. Woltersdorf, A. Brataas, R. Urban, and G. E. W. Bauer, *Phys. Rev.Lett.* **90**, 187601 (2003).
- ³⁵ K. Eid, R. Fonck, M. A. Darwish, W. P. P. Jr., and J. Bass, *J. Appl. Phys.* **91**, 8102 (2002).
- ³⁶ Y. Tserkovnyak, A. Brataas, and G. E. Bauer, *Phys. Rev.*

Lett. **88**, 117601 (2002).

³⁷ H. J. Carmichael, R. J. Brecha, M. G. Raizen, H. J. Kimble, and P. R. Rice, Phys. Rev. A **40**, 5516 (1989).

³⁸ M. Harder, L. Bai, P. Hyde, and C.-M. Hu, Phys. Rev. B **95**, 214411 (2017).

³⁹ M. Harder, Y. Yang, B. M. Yao, C. H. Yu, J. W. Rao,

Y. S. Gui, R. L. Stamps, and C.-M. Hu, Phys. Rev. Lett. **121**, 137203 (2018).

⁴⁰ S. M. Rezende, A. Azevedo, and R. L. Rodriguez-Suarez, Journal of Applied Physics **126**, 151101 (2019).

Supplementary Material for "Tunable magnon-magnon coupling in synthetic antiferromagnets"

I. SAMPLE CHARACTERIZATION BY VIBRATING SAMPLE MAGNETOMETER

In this study, we use the following free energy expression which includes of linear and quadratic exchange coupling contributions^{S1-S3} to describe static magnetisation direction in a synthetic antiferromagnet (SyAF):

$$F = \sum_{j=1}^2 \left[M_s \mathbf{B} \cdot \mathbf{m}_j + \frac{1}{2} M_s B_s (\mathbf{m}_j \cdot \mathbf{z})^2 \right] + \frac{2J_{ex1}}{d} \mathbf{m}_1 \cdot \mathbf{m}_2 + \frac{2J_{ex2}}{d} (\mathbf{m}_1 \cdot \mathbf{m}_2)^2. \quad (S1)$$

Here, M_s , \mathbf{B} , $\mathbf{m}_{1(2)}$, B_s , $J_{ex1(2)}$ are the saturation magnetisation, external magnetic field vector, the unit vector of individual moments in a SyAF, demagnetisation field, the linear and quadratic antiferromagnetic interlayer exchange coupling constants, respectively; d is the thickness of two ferromagnetic layers which are identical in the present case. Figure S1 shows magnetometry characterisation of two samples used in the present study. The red lines in the figure are calculated by using $M(B) = M_s \cos \phi(B)$ ^{S2-S4} where $\phi(B)$ is the angle between the applied magnetic field direction and equilibrium direction of individual moments which is obtained for all field values by minimizing Eq. S1 reiteratively until we achieve good matching to experimental data. The red curves in Fig. S1 were generated by the linear and quadratic exchange fields of 140 (30) ± 1.2 (0.6) mT and 7 (2) ± 0.1 (0.03) mT for the 0.5 (0.6) nm Ru thickness sample, together with $M_s = 1400$ (1300) kA/m for the 0.5 (0.6) nm Ru sample. The effective magnetic field acting on both moments can be given by differentiating the exchange coupling terms (F_{ex}) in Eq. S1 with respect to $\mathbf{m}_{1(2)}$:

$$B_{ex,1(2)} = -\frac{1}{2M_s} \frac{\partial F_{ex}}{\partial \mathbf{m}_{1(2)}} = -\frac{J_{ex1}}{d} \mathbf{m}_{2(1)} - \frac{2J_{ex2}}{d} (\mathbf{m}_1 \cdot \mathbf{m}_2) \mathbf{m}_{2(1)}, \quad (S2)$$

$\mathbf{m}_1 \cdot \mathbf{m}_2$ is a scalar value defined by the relative angle between \mathbf{m}_1 and \mathbf{m}_2 . Note that we incorporate this second-order exchange coupling term within B_{ex} for our analysis in our study.

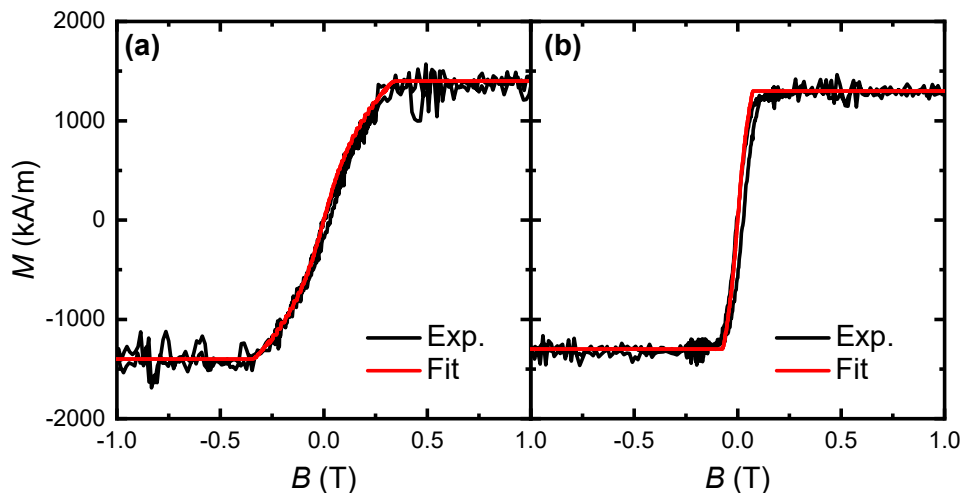


FIG. S1. (a-b) Magnetization curve of the CoFeB (3 nm)/Ru (t nm)/CoFeB (3 nm) measured by vibrating sample magnetometer for (a) $t = 0.5$ and (b) $t = 0.6$. The black (red) curve is the experimental (calculation) results.

II. ADDITIONAL MAGNETISATION-DYNAMICS RESULTS IN THIS STUDY

This section provides supplementary results used in our study to support our claims in the main text. In Fig. S2, we show 2D plots of frequency vs magnetic field for different θ_B from the sample with the Ru thickness of 0.5 nm. This supplements Fig. 2 in the main text and further supports our observation of crossing/avoided-crossing feature,

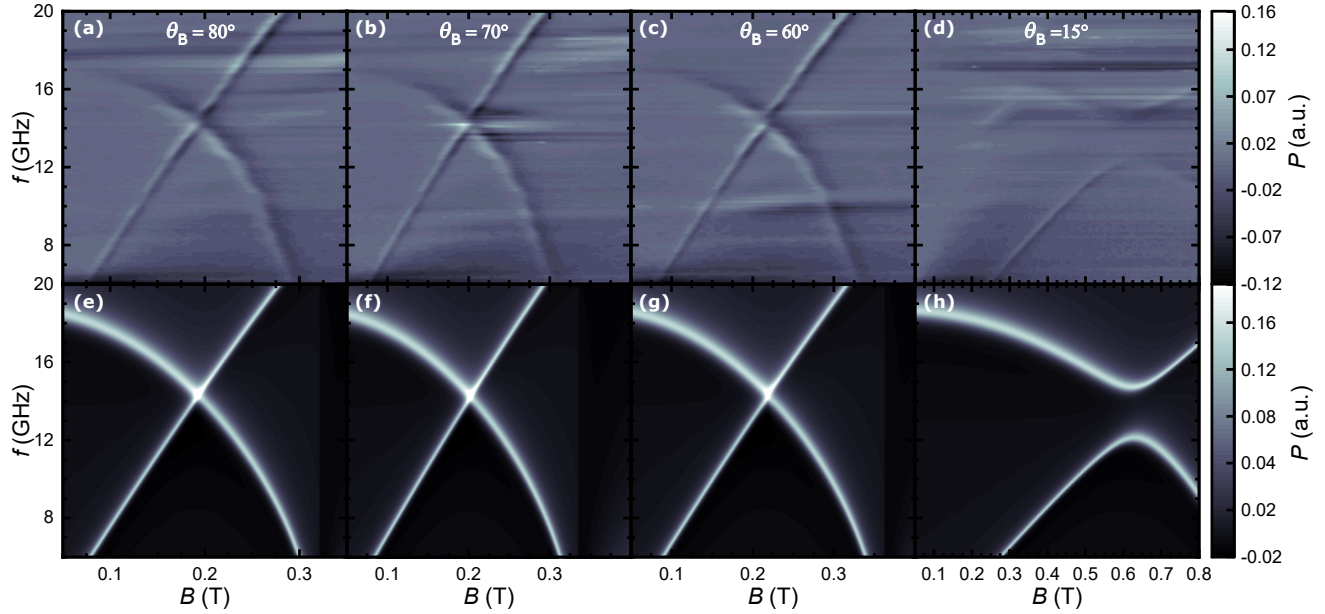


FIG. S2. (a-d) Extra data plots of Microwave transmission as a function of frequency and applied field, for the sample with the Ru thickness of 0.5 nm for different θ_B . Large coupling gap can be seen at low angles. Figures (e-h) plot simulation results for the same experimental conditions as Fig.(a-d).

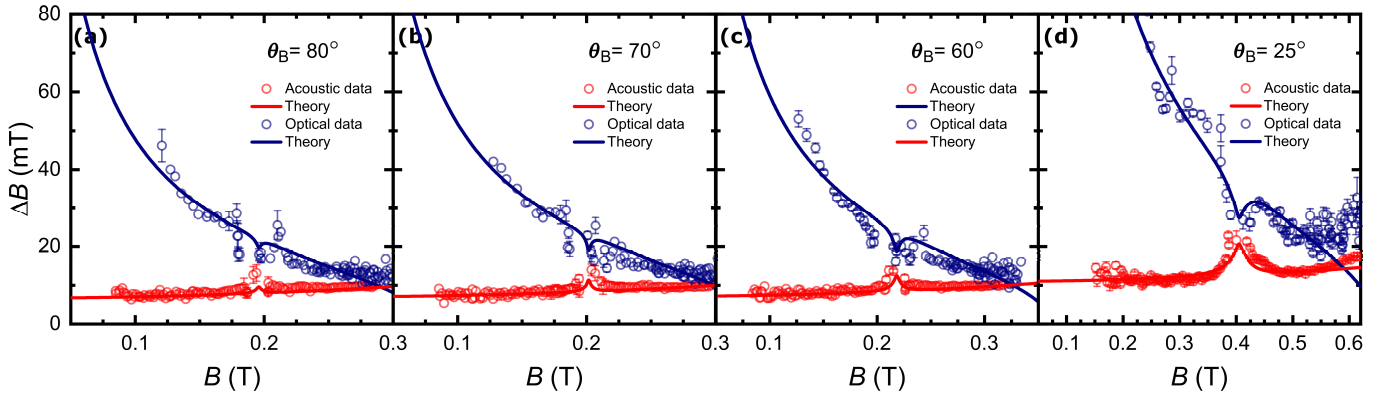


FIG. S3. (a-d) Extra data plots of linewidth of the two modes as a function of magnetic field for different θ_B for the sample with the Ru thickness of 0.5 nm. Solid lines represent simulation results from the theoretical model we used in this study.

controlled by the out-of-plane angle θ_B in the main text. Furthermore, Fig. S3 represents the magnetic-field-domain linewidth (ΔB) as a function of frequency measured for different θ_B . Theory curves plotted were produced by the imaginary part of eigenvalues discussed in the main text and Section 3 in this document. Damping parameters and loss rates plotted in Fig. 3(d) in the main text have been extracted from the parameters in the eigenvalue problem.

We repeated similar measurements for the sample with the Ru thickness of 0.6 nm. The same analysis procedure and plots have been carried out for experimental data and shown in Figs. S4 and S5. In Fig. S4, we notice that there exist magnetic-field independent background signals around 5 GHz which we consider as transmission losses unrelated to magnetisation dynamics. Nevertheless, we here highlight that the gap opening is much weaker than those measured for the sample with the Ru thickness of 0.5 nm. This is attributed to the size of exchange coupling, which has been independently quantified by VSM as explained above.

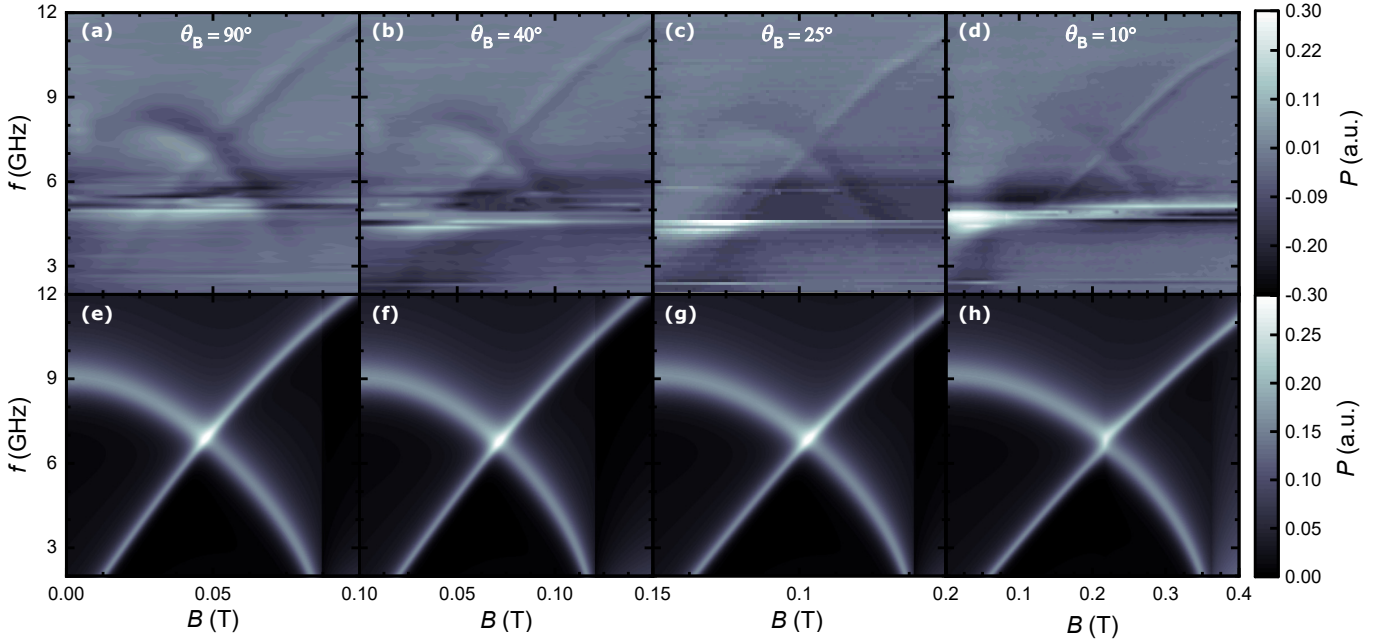


FIG. S4. (a-d) Microwave transmission as a function of frequency and applied field, for the sample with the Ru thickness of 0.6 nm for different θ_B . Small gap opening corresponds to the weak exchange coupling of the sample. Figures (e-h) plot simulation results for the same experimental conditions as Fig. (a-d).

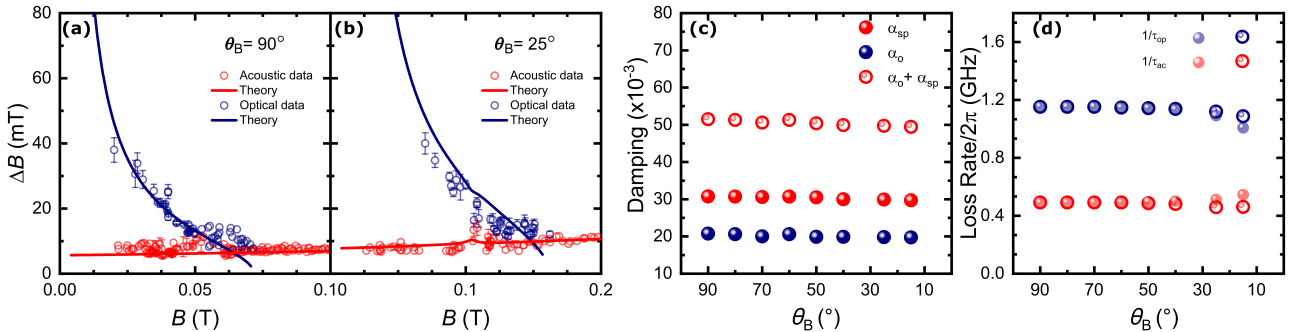


FIG. S5. (a-b) Linewidth of the two modes as a function of magnetic field for θ_B of (a) 90° and (b) 25° for the sample with the Ru thickness of 0.6 nm. We show our simulation results as solid lines. (c) Extracted values of damping parameters. (d) Calculated loss rates of each mode at the crossing point as well as those of the hybridised modes.

III. THE EIGENVALUE PROBLEM AND ANALYTICAL EXPRESSIONS

In this section, the two-coupled Landau-Lifshitz-Gilbert (LLG) equations at the macrospin limit are employed to model magnetic dynamics of optical and acoustic modes in SyAFs. We recognise that similar approaches have been taken by others previously^{S5-S7} but not specifically for magnon-magnon coupling phenomena in SyAFs as we detail below. We consider a canted regime of two individual moments (\mathbf{m}_1 and \mathbf{m}_2) which are coupled antiferromagnetically by the exchange interaction with the strength of B_{ex} . These two moments reside in thin-film magnets subjected to a demagnetisation field B_s and we apply an external magnetic field \mathbf{B} within the x - z plane with angle θ_B from the z axis which is the sample growth direction in our case. Following convention, we first define Kittel and Neel vectors as $\mathbf{m} = (\mathbf{m}_1 + \mathbf{m}_2)/2$ and $\mathbf{n} = (\mathbf{m}_1 - \mathbf{m}_2)/2$, respectively. Dynamics of these two coupled moments are given by^{S6}:

$$\frac{d\mathbf{m}}{dt} = -\Omega_L \mathbf{m} \times \mathbf{u} + \Omega_B [(\mathbf{m} \cdot \mathbf{z}) \mathbf{m} \times \mathbf{z} + (\mathbf{n} \cdot \mathbf{z}) \mathbf{n} \times \mathbf{z}] + \boldsymbol{\tau}_m, \quad (\text{S3})$$

$$\frac{d\mathbf{n}}{dt} = -\Omega_L \mathbf{n} \times \mathbf{u} + \Omega_B [(\mathbf{m} \cdot \mathbf{z}) \mathbf{n} \times \mathbf{z} + (\mathbf{n} \cdot \mathbf{z}) \mathbf{m} \times \mathbf{z}] + 2\Omega_{\text{ex}} \mathbf{n} \times \mathbf{m} + \boldsymbol{\tau}_n. \quad (\text{S4})$$

Here, $\Omega_L = \gamma B_0$, $\Omega_B = \gamma B_s$, and $\Omega_{\text{ex}} = \gamma B_{\text{ex}}$ where γ and B_0 are the gyromagnetic ratio and the resonance field, respectively; $\mathbf{u} = \sin\theta_B \mathbf{x} + \cos\theta_B \mathbf{z}$ represents the applied field direction in the x - z plane, given that \mathbf{x} and \mathbf{z} are unit vectors for the corresponding axes. The last terms in Eqs. (S4) and (S5) account for damping torques which are expressed as:

$$\boldsymbol{\tau}_m = \alpha_0 \left(\mathbf{m} \times \frac{d\mathbf{m}}{dt} + \mathbf{n} \times \frac{d\mathbf{n}}{dt} \right), \quad (\text{S5})$$

$$\boldsymbol{\tau}_n = (\alpha_0 + \alpha_{\text{sp}}) \left(\mathbf{m} \times \frac{d\mathbf{n}}{dt} + \mathbf{n} \times \frac{d\mathbf{m}}{dt} \right) - \alpha_{\text{sp}} \left[\mathbf{m} \cdot \left(\mathbf{n} \times \frac{d\mathbf{m}}{dt} \right) \frac{\mathbf{m}}{m^2} + \mathbf{n} \cdot \left(\mathbf{m} \times \frac{d\mathbf{n}}{dt} \right) \frac{\mathbf{n}}{n^2} \right], \quad (\text{S6})$$

where α_0 and α_{sp} are the standard Gilbert damping constant and one arising from mutual spin pumping between the two magnetic layers. With approximation of small angle precession, we can separate the equilibrium (\mathbf{m}_0 and \mathbf{n}_0) and time-dependent ($\delta\mathbf{m}(t)$ and $\delta\mathbf{n}(t)$) terms as $\mathbf{m}(t) = \mathbf{m}_0 + \delta\mathbf{m}(t)$ and $\mathbf{n}(t) = \mathbf{n}_0 + \delta\mathbf{n}(t)$ and here we define each vector component in a standard manner, *e.g.* $\mathbf{m}_0 = (m_{0x}, m_{0y}, m_{0z})$. Substituting $\mathbf{m}(t)$ and $\mathbf{n}(t)$ into Eqs. (S4)-(S7) and keeping the first order of the time-dependent and damping terms, we obtain the following six coupled equations:

$$\frac{1}{\Omega_B} \frac{d\delta m_x}{dt} = n_{0y} \delta n_z - \alpha_0 \eta (m_{0z}^2 + n_{0y}^2) \delta m_x - \eta m_{0z} \delta m_y + \alpha_0 (\eta + 1) m_{0x} m_{0z} \delta m_z, \quad (\text{S7})$$

$$\frac{1}{\Omega_B} \frac{d\delta m_y}{dt} = \alpha_0 m_{0z} n_{0y} \delta n_z + \eta m_{0z} \delta m_x - \alpha_0 \eta m_0^2 \delta m_y - (\eta + 1) m_{0x} \delta m_z, \quad (\text{S8})$$

$$\frac{1}{\Omega_B} \frac{d\delta m_z}{dt} = \alpha_0 \eta m_{0x} m_{0z} \delta m_x + \eta m_{0x} \delta m_y - \alpha_0 (\eta + 1) (m_{0x}^2 + n_{0y}^2) \delta m_z. \quad (\text{S9})$$

$$\frac{1}{\Omega_B} \frac{d\delta n_x}{dt} = (\alpha_0 + \alpha_{\text{sp}}) m_{0x} m_{0z} \delta n_z + \alpha_0 \eta n_{0y} m_{0x} \delta m_y + (\eta + 1) n_{0y} \delta m_z + \alpha_{\text{sp}} \frac{m_{0z} m_{0x} n_{0y}^2}{m_0^2} \delta n_z, \quad (\text{S10})$$

$$\frac{1}{\Omega_B} \frac{d\delta n_y}{dt} = -m_{0x} \delta n_z + \alpha_0 \eta m_{0x} n_{0y} \delta m_x + \alpha_0 (\eta + 1) m_{0z} n_{0y} \delta m_z, \quad (\text{S11})$$

$$\frac{1}{\Omega_B} \frac{d\delta n_z}{dt} = -(\alpha_0 + \alpha_{\text{sp}}) ((m_{0x}^2 + n_{0y}^2) \delta n_z - \eta n_{0y} \delta m_x + \alpha_0 \eta m_{0z} n_{0y} \delta m_y + \alpha_{\text{sp}} \frac{m_{0z}^2 n_{0y}^2}{m_0^2} \delta n_z), \quad (\text{S12})$$

where the equilibrium conditions and a new parameter η are introduced: $\mathbf{m}_0 = (m_{0x}, 0, m_{0z})$, $\mathbf{n}_0 = (0, n_{0y}, 0)$ and $\eta = 2\Omega_{\text{ex}}/\Omega_B$. Further simplification has been made by using additional parameter definitions as well as time derivative treatment:

$$\nu_{o1} = (\alpha_0 + \alpha_{\text{sp}}) (m_{0x}^2 + n_{0y}^2) - \alpha_{\text{sp}} \frac{m_{0z}^2 n_{0y}^2}{m_0^2} \quad (\text{S13})$$

$$\nu_{o2} = \alpha_0 \eta (m_{0z}^2 + n_{0y}^2), \quad (\text{S14})$$

$$\nu_{a1} = \alpha_0 \eta m_0^2, \quad (\text{S15})$$

$$\nu_{a2} = \alpha_0 (\eta + 1) (m_{0x}^2 + n_{0y}^2), \quad (\text{S16})$$

$$\frac{1}{\Omega_B} \frac{d}{dt} \rightarrow -i \frac{\omega}{\Omega_B} \equiv -i\Omega. \quad (\text{S17})$$

These produce the following equations of motion for δm_x , δm_y , δm_z and δn_z :

$$-i\Omega \delta m_x = n_{0y} \delta n_z - \nu_{o2} \delta m_x - \eta m_{0z} \delta m_y + \alpha_0 (\eta + 1) m_{0x} m_{0z} \delta m_z, \quad (\text{S18})$$

$$-i\Omega \delta m_y = \alpha_0 m_{0z} n_{0y} \delta n_z + \eta m_{0z} \delta m_x - \nu_{a1} \delta m_y - (\eta + 1) m_{0x} \delta m_z, \quad (\text{S19})$$

$$-i\Omega \delta m_z = \alpha_0 \eta m_{0x} m_{0z} \delta m_x + \eta m_{0x} \delta m_y - \nu_{a2} \delta m_z, \quad (\text{S20})$$

$$-i\Omega \delta n_z = -\nu_{o1} \delta n_z - \eta n_{0y} \delta m_x + \alpha_0 \eta m_{0z} n_{0y} \delta m_y. \quad (\text{S21})$$

We write these as a matrix form as follows.

$$\Omega \begin{pmatrix} \delta n_z \\ \delta m_x \\ \delta m_y \\ \delta m_z \end{pmatrix} = i \begin{pmatrix} -\nu_{o1} & -\eta n_{0y} & \alpha_0 \eta m_{0z} n_{0y} & 0 \\ n_{0y} & -\nu_{o2} & -\eta m_{0z} & \alpha_0 (\eta + 1) m_{0x} m_{0z} \\ \alpha_0 m_{0z} n_{0y} & \eta m_{0z} & -\nu_{a1} & -(\eta + 1) m_{0x} \\ 0 & \alpha_0 \eta m_{0x} m_{0z} & \eta m_{0x} & -\nu_{a2} \end{pmatrix} \begin{pmatrix} \delta n_z \\ \delta m_x \\ \delta m_y \\ \delta m_z \end{pmatrix} \quad (\text{S22})$$

We can obtain the eigen mode frequency $\omega_{op/ac}$ and relaxation time $\tau_{op/ac}$ by solving the complex eigenvalue problem, which can be expressed as,

$$\Omega_{op(ac)} = \frac{1}{\Omega_B} (\omega_{op(ac)} - i\tau_{op(ac)}^{-1}). \quad (\text{S23})$$

If we neglected damping terms in the off-diagonal components, we obtained the following relations:

$$\delta n_z \sim -\frac{\eta n_{0y}}{-i\Omega + \nu_{o1}} \delta m_x. \quad (\text{S24})$$

$$\delta m_z \sim \frac{\eta m_{0x}}{-i\Omega + \nu_{a2}} \delta m_y, \quad (\text{S25})$$

Using these relations, we reduced Eq. (S23) into an eigenvalue problem with a 2-by-2 matrix form given by:

$$\begin{pmatrix} \Omega^2 - \Omega_{op}^2 + i(\nu_{o1} + \nu_{o2})\Omega & -(-i\Omega + \nu_{o1}) \eta m_{0z} \\ (-i\Omega + \nu_{a2}) \eta m_{0z} & \Omega^2 - \Omega_{ac}^2 + i(\nu_{a1} + \nu_{a2})\Omega \end{pmatrix} \begin{pmatrix} \delta m_x \\ \delta m_y \end{pmatrix} = 0 \quad (\text{S26})$$

During this process, we disregarded higher-order terms in the diagonal elements, such as $\nu_{o1}\nu_{o2}$. This is the matrix we show in the main text after converting Ω into ω using Eq. S25. Here, Ω_{op} and Ω_{ac} are the eigen frequencies for optical mode and acoustic modes given by:

$$\Omega_{op} = n_{0y} \sqrt{\eta} - i \frac{1}{2} (\nu_{o1} + \nu_{o2}), \quad (\text{S27})$$

$$\Omega_{ac} = \sqrt{\eta^2 + \eta m_{0x}} - i \frac{1}{2} (\nu_{a1} + \nu_{a2}). \quad (\text{S28})$$

Equations (1) and (2) in the main text can be obtained by the real part of these two equations by using the equilibrium conditions: $(m_{0x}, m_{0y}, m_{0z}) = (B_0 \sin \theta_B / 2B_{ex}, 0, B_0 \cos \theta_B / (B_s + 2B_{ex}))$ and $(n_{0x}, n_{0y}, n_{0z}) = (0, \sqrt{1 - m_{0x}^2 - m_{0z}^2}, 0)$ with $\theta_B = \pi/2$. We note here that our numerical solutions of (S23) and (S27) are almost identical and therefore we decided to show the simpler 2×2 matrix in the main text. In order to provide the coupling constant g in the main text, we further take out the damping terms and solved the following eigen problem.

$$\begin{pmatrix} \Omega^2 - \Omega_{op}^2 & i\Omega \eta m_{0z} \\ -i\Omega \eta m_{0z} & \Omega^2 - \Omega_{ac}^2 \end{pmatrix} \begin{pmatrix} \delta m_x \\ \delta m_y \end{pmatrix} = 0 \quad (\text{S29})$$

$$(\Omega^2 - \Omega_{\text{op}}^2)(\Omega^2 - \Omega_{\text{ac}}^2) - \Omega^2(\eta m_{0z})^2 = 0 \quad (\text{S30})$$

By defining the crossing (dimensionless) frequency as $\Omega_{\text{op}} = \Omega_{\text{ac}} = \Omega_0$, we can find the energy gap ($\Delta\Omega_{\text{gap}}$) using Eq. (S32).

$$\Delta\Omega_{\text{gap}} = 2(\Omega - \Omega_0) = \pm \frac{2\Omega}{\Omega + \Omega_0} \eta m_{0z} \simeq \pm \eta m_{0z}, \quad (\text{S31})$$

Therefore,

$$g = \frac{1}{2} \Delta\Omega_{\text{gap}} \gamma B_s = \frac{\gamma B_{\text{ex}} B_0}{2B_s + 4B_{\text{ex}}} \cos\theta_B \quad (\text{S32})$$

Note that this is only valid when $\Delta\Omega_{\text{gap}} \ll \Omega_0$.

IV. IMPACT OF THE MUTUAL SPIN PUMPING DAMPING ON THE COUPLING

Our theory model allows to explore parameter regimes beyond experimental conditions. In an effort to understand the coupling of the two magnetic resonance modes in a SyAF, we investigated qualitatively the dependence of the damping parameters on the coupling strength. Especially, we focused on the effect of the damping arising from the mutual spin pumping between the two ferromagnets. This is because of our derived matrix form in Eq. S26 in which α_{sp} exists in the off-diagonal term, strongly suggesting that this parameter can contribute to the coupling of optical and acoustic modes. Figure S6 shows the simulated loss rate and resonance frequency of the acoustic and optic modes as a function of the magnetic field B for $\theta_B = 27^\circ$. The plots show the results of the full eigenvalue problem defined in Eq. S22 for several values of α_{sp} . For zero α_{sp} , the loss rate of the acoustic and optic mode cross at a lower magnetic field than the point of minimal frequency separation between the resonance frequencies of the two modes. With increasing α_{sp} , the crossing of the loss rates shifts higher in magnetic field until it appears at the same field as the minimal frequency separation of the resonance frequencies. For the highest α_{sp} the loss rate no longer cross and are separated. The dispersion of the resonance frequencies remains mostly unchanged for $\alpha_{\text{sp}} = 0$ and $\alpha_{\text{sp}} = 0.0255$. We observe that for higher α_{sp} , the coupling strength reduces and eventually goes to zero for the highest α_{sp} we

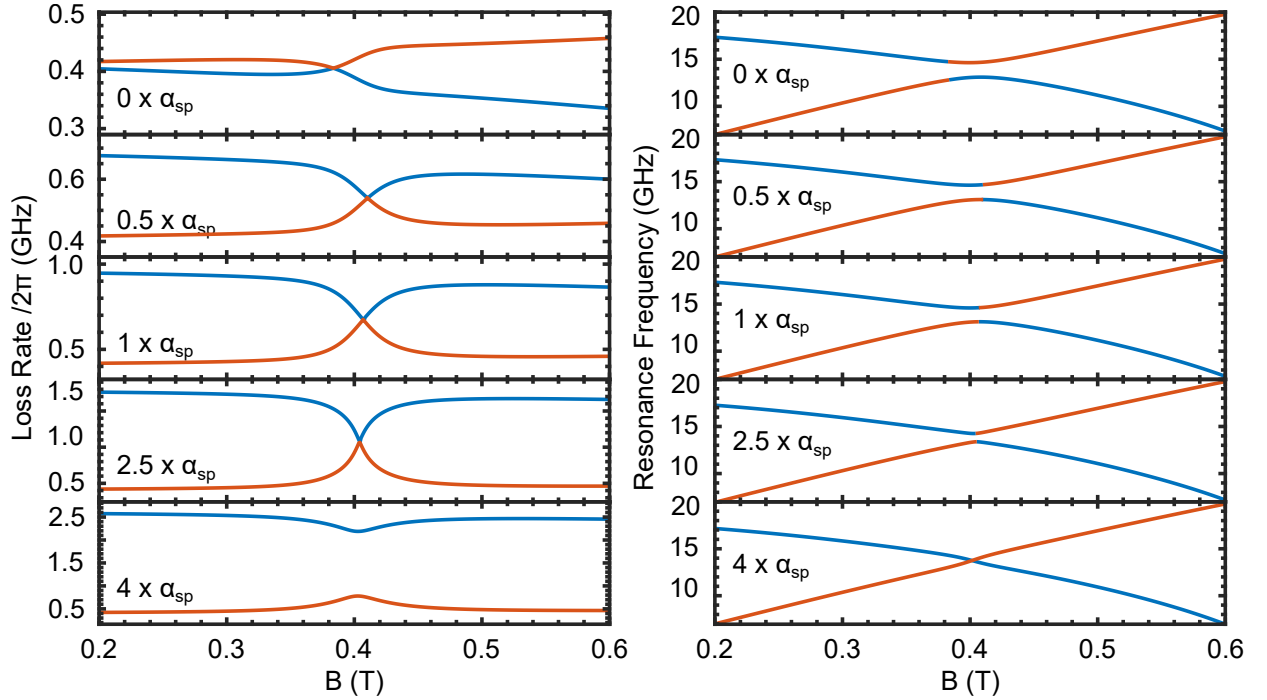


FIG. S6. Simulated loss rate (left panel) and resonance frequency (right panel) of the acoustic (red) and optic (blue) modes as a function of applied magnetic field at an angle of $\theta_B = 27^\circ$ for different multiples of the mutual spin pumping damping $\alpha_{\text{sp}} = 0.0255$. These are produced by solving Eq. S22 with other parameters of $B_s = 1.583$ T, $B_{\text{ex},1} = 0.14$ T, $B_{\text{ex},2} = 0.0065$ T, $\gamma/2\pi = 29$ GHz/T and $\alpha_0 = 0.0155$.

plot. From the change of the coupling strength with α_{sp} , we conclude that the coupling is partially mediated by spin currents. This change in the coupling behaviour can only be achieved by changing α_{sp} . In contrast, a change of the Gilbert damping α_0 has no influence on the coupling strength and only affects the loss rate of the modes. Our theory model suggests that the coupling between the acoustic and optic modes of a synthetic antiferromagnet is not fully described by a classical coupled harmonic oscillator model.

* aakanksha.sud.17@ucl.ac.uk

† h.kurebayashi@ucl.ac.uk

- [S1] S O Demokritov *J. Phys. D: Appl. Phys.* **31** 925 (1998).
- [S2] M. Belmeguenai, T. Martin, G. Woltersdorf, M. Maier and G. Bayreuther. *Phys. Rev. B* **76** 104414 (2007).
- [S3] S. Sorokin, R.A. Gallardo, C. Fowley, K. Lenz, A. Titova, G.P. Acheson, G. Dennehy, K. Rode, J. Fassbender, J. Lindner and A.M Deac *Phys. Rev. B* **101** 144410 (2020).
- [S4] S. M. Rezende, C. Chesman, M. A. Lucena, A. Azevedo, F. M. De Aguiar, and S. S. P. Parkin. *Journal of Applied Physics* **84** 958-972 (1998).
- [S5] D. MacNeill and J. T. Hou and D. R. Klein and P. Zhang and P. Jarillo-Herrero and L. Liu *Phys. Rev. Lett.* **123** 047204 (2019).
- [S6] T. Chiba, G. E. W. Bauer and S. Takahashi *Phys. Rev. B* **92** 054407 (2015).
- [S7] A. Kamimaki and S. Iihama and T. Taniguchi and S. Mizukami *Appl. Phys. Lett.* **115** 132402 (2019).